Fractal analysis reveals functional unit of ventilation in the lung

Bayat, Sam

2021-11

Bayat , S , Broche , L , Degrugilliers , L , Porra , L , Paiva , M & Verbanck , S 2021 , ' Fractal analysis reveals functional unit of ventilation in the lung ' , Journal of Physiology , vol. 599 , no. 22 , pp. 5121-5132 . https://doi.org/10.1113/JP282093

http://hdl.handle.net/10138/351556
https://doi.org/10.1113/JP282093

unspecified
acceptedVersion

Fractal Analysis Reveals Functional Unit of Ventilation in the Lung

S. Bayat[1,2], L. Broche[3], b, L. Degrugilliers[4], L. Porra[5], M. Paiva[6] and S. Verbanck[7]

[1] Grenoble University Hospital, Department of Pulmonology & Physiology, Grenoble, France

[2] STROBE Laboratory, Univ. Grenoble-Alps, INSERM UA7, Grenoble, France

[3] European Synchrotron Radiation Facility, Biomedical Beamline, Grenoble, France

[4] Amiens University Hospital, Amiens, France.

[5] University of Helsinki Department of Physics, & Helsinki University Central Hospital, Finland

[6] University Hospital Erasme, Université Libre de Bruxelles, Brussels, Belgium

[7] University Hospital UZ, Respiratory Division, Brussels, Belguim

Corresponding author: Prof. Sam Bayat MD PhD
Department of Pulmonology & Physiology,
Grenoble University Hospital, Bd. Du Maquis du Grésivaudan,
38700, La Tronche, France

Email: sbayat@chu-grenoble.fr

Running title: Imaging the functional Unit of ventilation in the lung.

Abstract

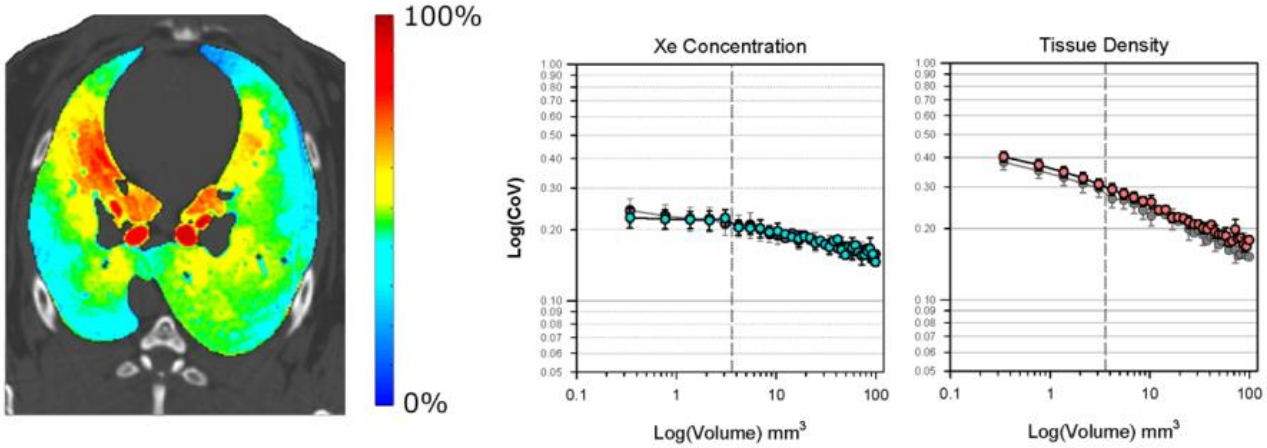

Ventilation is inhomogeneous in the lungs across species. It has been hypothesized that ventilation inhomogeneity is largely determined by the design of the airway branching network. Because exchange of gases at the alveolar barrier is more efficient when gas concentrations are evenly distributed at subacinar length scales, it is assumed that a "functional unit" of ventilation exists within the lung periphery, where gas concentration becomes uniform. On the other hand, because the morphology of pulmonary airways and alveoli, and the distribution of inhaled fluorescent particles show self-similar fractal properties over a wide range of length scales, it has been predicted that fractal dimension of ventilation approaches unity within an internally homogenous functional unit of ventilation. However, the existence of such a functional unit has never been demonstrated experimentally due to lack of *in situ* gas concentration measurements of sufficient spatial resolution in the periphery of a complex bifurcating network. Here, using energy-subtractive synchrotron radiation tomography, we measured the distribution of an inert gas (Xe) in the *in vivo* rabbit lung during Xe washin breathing manoeuvres. The effects of convective flow rate, diffusion, and cardiac motion were also assessed. Fractal analysis of resulting gas concentration and tissue-density maps revealed that fractal dimension was always smaller for Xe than for tissue density, and that only for the gas, a length scale existed where fractal dimension approached unity. The length scale where this occurred was seen to correspond to that of a rabbit acinus, the terminal structure comprising only alveolated airways.

Keywords: Pulmonary ventilation; Synchrotrons; Fractal analysis; Xenon.

Key Points

- Gas ventilation is inhomogeneous in the lung of many species. However, it is not known down to what length scales this inhomogeneity persists.
- It is generally assumed that ventilation becomes homogenous at subacinar length scales, beyond the spatial resolution of available imaging techniques but this has not been demonstrated experimentally.
- Here we imaged the distribution of inhaled Xe gas in the rabbit lung using synchrotron radiation energy-subtractive imaging and used fractal analysis to show that ventilation becomes internally uniform within regions about the size of rabbit lung acini.

Introduction

Regional lung ventilation is inhomogeneous in the normal lung across many species (Verbanck & Paiva, 2011). The inhomogeneity in lung ventilation dramatically increases in disease conditions. Differences in ventilation between lung units can arise between lung lobes, subsegments or between air sacs where all airways are alveolated, termed acini (Verbanck & Paiva, 2011). Resulting gas concentration differences are convection-dependent and mainly determined by differences in the regional mechanical time constant between lung units resulting from differences in regional compliance or airway resistance, which are not evenly distributed even among isogravimetric lung regions (Glenny & Robertson, 2011).

Ventilation can also be inhomogeneous at smaller length scales, within the acini. Early on and using hydrogen as a tracer gas (Krogh & Lindhard, 1914), it was observed experimentally that the alveolar concentrations of this gas varied during exhalation. Since that observation, experiments performed by direct sampling of gas in small airways (Engel *et al.*, 1974), in microgravity (Prisk *et al.*, 1998), using positron emission tomography (Valind *et al.*, 1991), hyperpolarized Helium magnetic resonance imaging (Horn *et al.*, 2014), or using deposition of fluorescent microspheres as a surrogate measure (Altemeier *et al.*, 2000) have indicated that in the mammalian lung, part of ventilation heterogeneity finds its origin in the lung periphery, beyond the resolution of commonly available ventilation imaging modalities.

Beyond the challenge of direct measurement of gas concentrations within a complex bifurcating structure, the study of the inhomogeneity in lung ventilation is complicated by the fact that this inhomogeneity depends on the scale of resolution. Both the branching structure of pulmonary airways (West *et al.*, 1986; Haefeli-Bleuer & Weibel, 1988) and alveoli (Tanabe *et al.*, 2020) have been shown to have self-similar, fractal properties over a wide range of length scales. As a general rule, spatial inhomogeneity of a measured quantity q, representing an intrinsic characteristic in a self-similar fractal system, is a power law of the spatial length scale d, or resolution at which the measurement is performed, such that:

$$\frac{q}{q_0} = \left(\frac{d}{d_0}\right)^{\left(1-D_f\right)} \quad (1)$$

Where D_f is fractal dimension, obtained from the slope of the log-log plot of q (inhomogeneity) as a function of length scale. Fractal analysis therefore allows describing scale-dependent inhomogeneity, by a scale-independent fractal dimension.

Since exchange of gases at the alveolar-capillary barrier is more efficient when gas concentrations are evenly distributed, it is generally assumed that a uniform "functional unit" exists within the lung periphery, where molecular diffusion promotes equilibration of gas concentrations. Hence refinements in spatial resolution of the measurement in gas distribution may not show further differences in inhomogeneity which should be reflected in a D_f approximating unity (Altemeier *et al.*, 2000). Thus far, the existence and size of such a functional gas-exchanging lung unit has not been demonstrated experimentally. Fractal analysis of gas distribution within the lung structure has not been pursued as extensively as fractal analysis of bronchial structures. This is mainly because direct measurement of gas distribution down to acinar resolutions is extremely challenging and those ventilation imaging modalities that do allow a quantitative assessment lack sufficient spatial resolution. In one study using local fluorescent aerosol deposition in pig lungs as a surrogate for gas ventilation, a fractal dimension of 1.16 was obtained, and it was suggested that at the acinar scale, beyond the spatial resolution of their measurement method, D_f would drop to unity (Altemeier *et al.*, 2000).

Here we hypothesized that using synchrotron imaging in a rabbit lung, it is possible to identify the size of a functional lung unit of gas transport, signalled by a drop in the fractal dimension as the scale of resolution is reduced. We used a synchrotron radiation energy-subtractive imaging technique to measure the spatial distribution and heterogeneity of ventilation using an inhaled inert gas: Xe, in *in vivo* rabbit lungs. We further assessed the effect of flow rate, and potential contribution of cardiac motion to gas mixing on the fractal dimension D_f of both gas distribution and lung tissue density.

Materials and Methods

Ethical approval

Experiments were in accordance with the Directive 2010/63/EU of the European Parliament on the protection of animals used for scientific purposes (EU, 2010) and complied with the ARRIVE guidelines (Percie du Sert *et al.*, 2020) and were approved by the national Evaluation Committee for Animal Welfare in Research (Ethax#113) under the number APAFIS-2015091517388915. All steps were taken to minimise the animals' pain and suffering. Animals were housed at the Biomedical Facility of the Biomedical Beamline of the European Synchrotron Radiation Facility (ESRF) with ad libitum access to food and water.

Animal preparation

Experiments were performed in 8 anesthetized and mechanically ventilated male New-Zealand White rabbits (2.9 ± 0.2 kg), purchased from a commercial breeder (Charles River Laboratories, Écully, France). Anaesthesia was

induced by IV injection of thiopental sodium (25 mg/kg) via a catheter (22 G) introduced into the marginal ear vein under local anaesthesia (5% topical lidocaine). Additional half doses of anaesthetic were administered as required to maintain full surgical anaesthesia during animal preparation. The animal was tracheotomised with a no. 3 Portex tube (Smiths medical, Kent, United Kingdom) and was mechanically ventilated in a custom-built system incorporating image acquisition, as described previously (Bayat *et al.*, 2001). Anaesthesia was maintained with 0.1 mg/kg/h IV midazolam. After ensuring adequate anaesthesia by ensuring loss of motor response to noxious stimulus to the paw , paralysis was induced by continuous IV infusion of atracurium (1.0 mg/kg/h). Depth of anaesthesia was monitored by regularly assessing the state of the pupils. The animal was placed in a custom-made plastic holder for imaging in upright position as described previously (Bayat *et al.*, 2009). Prior to post-mortem imaging, the animals were euthanised by intravenous thiopental sodium overdose (220 mg/kg).

K-edge subtraction imaging

The experiments were performed at the ESRF. The K-edge subtraction computed tomography (KES-CT) technique allows simultaneous imaging of the lung tissue, and the concentration (mass per unit of volume) of inhaled Xenon gas within the airspaces. The instrumental setup has been described previously (Suortti *et al.*, 2000). This imaging technique uses two monochromatic X-ray beams at slightly different energies bracketing the Xe K-edge, at 34.56 keV. Visualization and quantitative measurement of Xe concentration within the airways is based on the property that the attenuation coefficient of Xe increases by a factor of 5.4 when the energy of the incident X-ray beam exceeds the Xe K-edge. X-rays from a synchrotron radiation source are required because, as opposed to standard X-ray sources, they allow the selection of monochromatic beams from the full X-ray spectrum while conserving enough intensity for imaging with sufficient temporal resolution. The horizontal beams, 98 mm wide and 0.6 mm in height, are focused on the animal (Figure 1A). KES-CT imaging is performed in parallel-beam geometry. Two CT images are simultaneously acquired during the Xe inhalation manoeuvre, using a liquid nitrogen cooled Germanium detector with a pixel size of 350 µm. The effective detector resolution has previously been characterized in (Peterzol *et al.*, 2003). The image slice thickness was determined by the radiation beam height of 700 µm. Each CT image consisted in 720 projections over 360° per 1.5 s. CT images were reconstructed using a filtered back projection algorithm with resulting voxel dimensions of 350×350×700 µm. Using the dual-energy KES synchrotron imaging method, X-ray attenuation by tissue density and Xe concentration is computed separately, using a custom material decomposition algorithm as described previously (Bayat *et al.*, 2001). X-rays from a synchrotron radiation source are required because as opposed to standard X-ray sources, they allow the selection of monochromatic beams from the full X-ray spectrum while conserving enough intensity for imaging with sufficient temporal resolution.

Study protocol

Following a stabilization period of 10 to 15 min, a 2D projection image was acquired and used to select 2 axial CT image levels, one at the 5th ("apical") and one at the 8th ("basal") vertebral level. Besides a reference breathing manoeuvre performed on all animals, additional manoeuvres were designed to specifically study the effect of (convective) flow rate and molecular diffusion, on Xe and tissue density inhomogeneity at various length scales. The reference manoeuvre consisted of a single breath Xe washin (SBW) starting at end-expiration (functional residual capacity) with 11 images acquired at 1.5 s intervals during continuous inhalation. In SBW manoeuvres, maximal pressure was limited to 30 cmH_2O using an overpressure valve. The image corresponding to the onset of the inspiratory pause was selected for analysis.

Next, a multiple breath washin (MBW) was performed. with an approximately ten-fold flow rate, followed by an inspiratory pause of 3s during which a CT image was acquired, and a 4 s exhalation (Figure 1B). This breathing cycle was repeated 12 times, where the animal was administered air for 2 cycles and Xe for the 10 subsequent ones, and then switched back to air. hence, the 3rd image corresponded to an equivalent inhaled volume as in the reference SBW manoeuvre, and was selected for analysis.

In order to assess the potential effect of cardiac motion on Xe gas distribution inhomogeneity, SBW and MBW manoeuvres were repeated immediately after euthanasia. The animal was euthanized by IV injection of pentobarbital sodium (220 mg/kg). Cardiac arrest was verified by the lack of cardiogenic oscillations on the respiratory flow signal and by the tissue-density KES-CT images. Image acquisition was then resumed, performing both SBW and MBW manoeuvres immediately post-mortem. In order to test the impact of diffusion, on a subset of 5 animals, SBW manoeuvres were performed with lower (slow-SBW-BH) and higher (fast-SBW-BH) inspiratory flow rate, followed by an inspiratory pause. Images were repeatedly acquired during this pause (8 images at 1.5 s intervals Figure 1B).

Image processing

The lungs were segmented from the surrounding tissues in the 2D tissue-density KES-CT images using a density-based thresholding algorithm (Otsu, 1979) and converted to a binary mask. The mask was then applied to Xe-density images in order to obtain a Xe concentration map (Figure 1) and a tissue density map within identical regions. Not a number (NaN) values were assigned to background voxels.

A grid of increasing box size starting at 2×2 voxels (=4×0.35×0.35×0.70=0.343 mm^3) and incremented stepwise 30 times, was randomly placed on the tissue-density or Xe concentration maps. The coefficient of variation (standard deviation/mean) of tissue density or Xe was computed within each box and averaged for the entire map. The log(CoV) of Xe or tissue density was then plotted as a function of log(box volume). All image processing and computations were performed using custom written code in Matlab (Mathworks, Natick, MA, USA).

A piecewise polynomial function was fitted to the aforementioned log-log plots using Sigmaplot software (Systat Software V.13, Inpixon UK) to verify the box size at which a breakpoint occurred in the Xe log-log plots. From this, two values D_f were determined as one minus the slope of the log-log plot in its portion on either side of the breakpoint.

Statistical analysis

Data are expressed as mean ± standard deviation. A general linear multiple regression model was used, with D_f as dependent variable, fixed effects including regional size (acinar vs. extra-acinar), level (apical vs. basal), animal status (live vs. post-mortem), type of manoeuvre (*SBW*, *MBW*, *BH*), type of contrast (Xe vs. Tissue density), and individual rabbits as a random effect. A Tukey post-hoc multiple comparison procedure was performed to analyse significant interactions between fixed effects on D_f. Overall, n=128 (8 animals; 2 contrasts: *Xe, Tissue*; 2 image levels; 2 conditions: *in vivo, post mortem*; 2 regional sizes: *acinar, extra-acinar*) for the reference *SBW* manoeuvre, and n=332 when including additional *fast* and *slow* flow rate manoeuvres. Changes in D_f with time during breath hold (n=10; 5 animals × 2 image levels), were assessed by Friedman repeated-measures analysis of variance on ranks for each contrast (Xe, Tissue) and region (acinar, axtra-acinar). A $p<0.05$ was considered significant. The statistical analysis was performed with *R* (Version 1.2.1335, https://www.R-project.org) (R, 2020).

Results

Data are obtained in 8 anesthetized and mechanically ventilated male New-Zealand White rabbits. Inhaled gas flows and volumes during the various breathing manoeuvres are summarized in Table 1. Sample composite images from a reference SBW manoeuvre in one animal are shown in Figure 1C. The dynamics of Xe concentration within the airspaces obtained by synchrotron imaging during a sample SBW manoeuvre is shown in supporting video S1. Gas concentration (Xe) and tissue density data for different time points during the inhalation phase of the reference manoeuvre (SBW) are shown in Figure 2. As expected, tissue density is seen to decrease as the lung inflates, while Xe concentration is seen to gradually increase. Corresponding CoV curves also differ between gas and tissue, in that overall CoV for tissue density for the smallest ROI volumes increases with time, whereas CoV decreases as concentration differences between the trachea and the lung periphery attenuate and stabilize through continued inhalation. Logarithmic plots of CoV of regional Xe concentration and tissue density versus region of interest volume for the reference SBW manoeuvre in one image level *in vivo* are shown in Figure 3.

For fractal analysis of gas and tissue density in the reference SBW manoeuvre, and subsequent analysis including different manoeuvres, only end-inspiratory images were considered (e.g.: violet curves in Figure 2 C, D). For Xe, a distinct flattening of the log-log plot was identified towards the smaller ROI volumes, which was less apparent for tissue-density. Using all log-log plots from the reference SBW manoeuvre, a piecewise polynomial fit of individual Xe plots identified a threshold volume of 3.8±3.3 mm^3 below which the flattening occurred. Consequently, we computed a fractal dimension termed *acinar* D_f from the slope of the log-log plot in the size range 0.34 to 3.1 mm^3 (corresponding to the 2×2 to 5×5 voxel ROI). In the size range 4.2 mm^3 to 100 mm^3 (corresponding to the 6×6 to 33×33 voxel ROI), *extra-acinar* D_f was computed. Acinar and extra-acinar D_f values for the reference SBW manoeuvre, including data from both axial image levels (*apical*, *basal*) and both animal states (*post-mortem*, *in vivo*), for both Xe and tissue-density, are shown for each animal in Figure 4A. The generalized mixed linear regression model, with fixed effects including “region” (acinar vs. extra-acinar), “axial level” (apical vs. basal), “status” (live vs. post-mortem), type of “contrast” (Xe vs. tissue density), showed significance for “region” ($p<0.0001$), “contrast” ($p<0.0001$), and for interaction between “region” and “axial level” ($p<0.0001$). Acinar D_f of Xe ($D_{f,Xe}$) was seen to approach unity, and was significantly smaller than extra-acinar $D_{f,Xe}$. Because there was a significant interaction between region and axial level, we performed a post-hoc Tukey multiple comparisons analysis within each axial imaged level, to confirm that the region effect (acinar versus extra-acinar D_f) remained significant. This was the case for both Xe and tissue density. In addition, $D_{f,Xe}$ was significantly smaller than *Df* of tissue density ($D_{f,tissue}$), in both acinar and extra-acinar regions (Figure 4A). A boxplot summarizing these findings for the SBW manoeuvre is shown in Figure 4B. Since *in vivo* and *post-mortem* results (identified in Figure 4A) were not significantly different, these were combined in the boxplot. Repeating the generalized mixed linear regression model analysis on all SBW and MBW manoeuvres combined,

and adding flow rate (*slow* vs *fast*) as an additional fixed affect, did not change the outcome, in that "region", "contrast" and interaction between "region" and "axial level" were still significant, while flow rate did not add a significant effect; the graph summarizing all SBW and MBW results is shown in Figure 5. Finally, with breathhold the acinar $D_{f,Xe}$ tended towards 1, unlike extra-acinar $D_{f,Xe}$ which gradually decreased with BH time (Figure 6).

Discussion

Here we demonstrate for the first time, that regional distribution of inert gas concentration in the *in vivo* mammalian lung is fractal with a $D_{f,Xe}$ of approximately 1.1 across the range of length scales exceeding the acinar gas exchanging units, and that $D_{f\ Xe}$ is significantly smaller and approaches unity at acinar length scales. At both length scales, $D_{f,Xe}$ is consistently smaller than $D_{f,tissue}$.

The fractal nature of ventilation observed here is in agreement with previous reports where overlapping extra-acinar length scales offer a means of comparison. The extra-acinar $D_{f,Xe}$ value was similar to the 1.16 value previously measured by Altemeier et al. (Altemeier *et al.*, 2000) where aerosolized 1 µm florescent microsphere deposition could be assessed down to 1.5 cm^3 resolution, using precision cut dices from post mortem pig lungs. Despite criticism concerning the ability of micron particles to perfectly mimic distribution of a gas, the comparison between D_f obtained with aerosol or with an inert gas at extra-acinar length scales is probably legitimate. Even if micron particle distribution data had been available, a direct comparison might have been compromised within the acinus where gas and aerosol transport have been shown to follow different rules (Tsuda *et al.*, 2002). In any case, no other data on direct in-situ measurement of gas concentration distribution at acinar scale in a mammal are available to date. With morphometric studies of the rabbit lung anatomy reporting an acinar size range of 3-5mm^3 (Rodriguez *et al.*, 1987), the voxel size of our synchrotron radiation imaging technique of 0.086 mm^3 was sufficiently small to interrogate intra-acinar gas heterogeneity. Our method also allowed us to show a distinct difference in fractal properties between lung tissue structure and the ventilation within it.

Xe is a soluble gas. *In vivo*, blood concentrations typically reach ~16% of that within the parenchyma (based on data from 5 animals; data not shown) by the end of the SBW inhalation. This range of blood concentration is in line with previous measurements of Xe gas/blood partition coefficients (Chen *et al.*, 1980). Post-mortem, blood Xe concentrations fell to very low values (~3%). We do not expect that the diffusion of Xe from the lung acini to blood affected the Df of Xe, since we did not find a significant difference in $D_{f,Xe}$ between in vivo and post mortem images. Also, the concern that Xe disappearing from the airspaces into blood and tissue would affect its capacity to be a marker of regional ventilation is offset by the fact that Xe dilution in the tissue phase is proportional to the concentration in the gas phase. Hence, even if absolute Xe concentration values might be affected by this phenomenon, the distribution and heterogeneity of ventilation is unlikely to be significantly affected.

In the present study, we assessed the fractal dimension of specific ventilation in thin slices of the lung which result in 2D images. A 2D plane of a 3D process can accurately estimate the fractal properties of the spatial process as demonstrated by previous studies in the literature (Paumgartner *et al.*, 1981; Venegas & Galletti, 2000; Andersen *et al.*, 2012; Porzionato *et al.*, 2016; Tanabe *et al.*, 2020).

Theoretical studies suggest that the ¼ allometric scaling law of structural and functional parameters to body size across all living organisms is explained by the fractal design of branching linear transport networks (West *et al.*, 2002). This is based on the assumptions that the branching network must supply the entire organ or organism, that the energy required to distribute resources is minimized, and that the final branch of the network is a size-invariant unit (West *et al.*, 1997). In the lung, both the airway tree (West *et al.*, 1986) and alveoli (Porzionato *et al.*, 2016) exhibit self-similar fractal properties. In the present study, we also found tissue density to be fractal (Figure 2). Despite being smaller within acini than in extra-acinar regions, $Df_{,tissue}$ exceeded unity in all instances. In addition, $D_{f\ Xe}$ was consistently smaller than $Df_{,tissue}$, both at acinar and extra-acinar length scales.

Over most of the length scales studied, gas concentration heterogeneity is seen to increase as the measurement length scale is reduced, but at acinar length scale this behaviour is altered. The significance of a D_f of inert gas concentration approaching 1 within lung units of acinar size, signals that gas concentration within these units is almost perfectly spatially correlated, and internally homogeneous, at least in a normal lung. Our findings could be explained by the fact that the fractal nature of regional lung ventilation distribution results from that of the airway network with the recursive self-similar branching. This implies that ventilation distribution over increasingly smaller airways is determined essentially by the regional mechanical time constants, governing convective gas transport. However, the significantly smaller $D_{f,Xe}$ almost reaching unity within acini, suggests that at acinar level different underlying processes determine ventilation distribution and heterogeneity. The most obvious reason for this is that molecular diffusion will promote homogenization of any gas concentration differences that might have arisen within acini. Also, any residual inhomogeneity of gas concentration in a given sub-acinar unit is likely far more similar to that in the adjacent unit than to a spatially distant one. The fact that sequential imaging during a breath-hold manoeuvre showed that the acinar $D_{f,Xe}$ tended towards 1 (Figure 6) while the extra-acinar $D_{f,Xe}$ gradually decreased may have been due to the diffusion of Xe, considering that with a 0.1 cm^2/s diffusing coefficient, Xe can cover 4.5mm over 1s by molecular diffusion.

Since diffusion is a physical process associated with concentration homogenization, it is generally assumed that it contributes to a uniform distribution of gas concentration within lung acini. However, modelling and experimental studies have also indicated that in the transitional zone between the non-alveolated bronchi and alveolated intra-acinar airways, where diffusion and convection compete, intra-acinar gas concentration differences may arise,

because of the asymmetry of the intra-acinar branching structure (Paiva & Engel, 1979). For gases that are not biologically inert, an additional concept termed diffusional screening of O_2 diffusing across the blood-gas barrier has been suggested to induce intra-acinar O_2 concentration differences (Sapoval *et al.*, 2002), even though subsequent modelling has minimized its role under normal physiological conditions (Swan & Tawhai, 2011). Irrespective of the exact mechanism of any residual peripheral gas heterogeneities, it does appear that the dramatic structural change from bifurcating smooth-walled airways to alveolated bifurcating air spaces induces a concomitant change in fractal properties of gas concentration distribution.

Flow rate did not significantly affect $D_{f,Xe}$ and $D_{f,tissue}$ behavior at acinar or extra-acinar length scales. There was an impact of axial image level on *Df*, which could have been related to gravity and to the proximity of heart and diaphragm in level L2. However, overall $D_{f,Xe}$ and $D_{f,tissue}$ behavior was maintained, and the absence of any significant effect from live vs post mortem status indicates that heart beat or the use of blood soluble Xe per se did not affect D_f.

In conclusion, we used energy-subtractive synchrotron radiation imaging to map the distribution of ventilation using an inert gas: Xe, within the lung airspaces with a subacinar resolution. We found that the regional distribution of ventilation in the lung is fractal. The fractal dimension D_f of Xe is itself dependent on length scale; it significantly decreases to approach 1 below a threshold volume that is close to the average acinar volume, which was not the case for the D_f of tissue density. This suggests that a "functional unit of ventilation" exists within the normal lung acini, where ventilation inhomogeneity becomes scale invariant and quasi-perfectly spatially correlated. This corresponds to the length scale where molecular diffusion is the predominant gas transport mechanism. The fractal dimension of ventilation was not dependent on flow velocity, cardiogenic mixing or gravity.

Additional Information

Data availability: Data are available upon reasonable request to the corresponding author.

Competing Interests: The authors declare no competing interests in relation to the present work.

Author Contributions: SB, MP and SV designed and planned the study; SB, LB and SV acquired the data; SB, LB, LD and SV analyzed the data; SB and SV drafted the manuscript; all authors took part in the interpretation, critical revision and final approval of the manuscript.

Funding: This study was supported by the European Synchrotron Radiation Facility (MD1010). Sam Bayat was supported by the European Regional Development Fund #REG08009 via the Picardie Regional Council (Amiens, France).

Acknowledgments: The authors wish to thank Herwig Requardt, Alberto Bravin and ESRF ID-17 staff for technical assistance.

References

Altemeier WA, McKinney S & Glenny RW. (2000). Fractal nature of regional ventilation distribution. *J Appl Physiol (1985)* **88,** 1551-1557.

Andersen MP, Parham AR, Waldrep JC, McKenzie WN & Dhand R. (2012). Alveolar fractal box dimension inversely correlates with mean linear intercept in mice with elastase-induced emphysema. *Int J Chron Obstruct Pulmon Dis* **7,** 235-243.

Bayat S, Duc GL, Porra L, Berruyer G, Nemoz C, Monfraix S, Fiedler S, Thomlinson W, Suortti P, Standertskjöld-Nordenstam CG & Sovijärvi ARA. (2001). Quantitative functional lung imaging with synchrotron radiation using inhaled xenon as contrast agent. *Physics in medicine and biology* **46,** 3287-3299.

Bayat S, Strengell S, Porra L, Janosi TZ, Petak F, Suhonen H, Suortti P, Hantos Z, Sovijarvi AR & Habre W. (2009). Methacholine and ovalbumin challenges assessed by forced oscillations and synchrotron lung imaging. *Am J Respir Crit Care Med* **180,** 296-303.

Chen RY, Fan FC, Kim S, Jan KM, Usami S & Chien S. (1980). Tissue-blood partition coefficient for xenon: temperature and hematocrit dependence. *J Appl Physiol Respir Environ Exerc Physiol* **49,** 178-183.

Engel LA, Utz G, Wood LD & Macklem PT. (1974). Ventilation distribution in anatomical lung units. *J Appl Physiol* **37,** 194-200.

EU. (2010). Directive 2010/63/EU of the European parliament and of the council of 22 September 2010 on the protection of animals used for scientific purposes. *OJ European Union* **L276**.

Glenny RW & Robertson HT. (2011). Spatial distribution of ventilation and perfusion: mechanisms and regulation. *Comprehensive Physiology* **1,** 373-395.

Haefeli-Bleuer B & Weibel ER. (1988). Morphometry of the human pulmonary acinus. *The Anatomical record* **220,** 401-414.

Horn FC, Deppe MH, Marshall H, Parra-Robles J & Wild JM. (2014). Quantification of regional fractional ventilation in human subjects by measurement of hyperpolarized 3He washout with 2D and 3D MRI. *J Appl Physiol (1985)* **116,** 129-139.

Krogh A & Lindhard J. (1914). On the average composition of the alveolar air and its variations during the respiratory cycle. *J Physiol* **47,** 431-445.

Otsu N. (1979). A threshold selection method from gray-level histograms. *IEEE transactions on systems, man, and cybernetic* **9,** 62-66.

Paiva M & Engel LA. (1979). Pulmonary interdependence of gas transport. *J Appl Physiol Respir Environ Exerc Physiol* **47,** 296-305.

Paumgartner D, Losa G & Weibel ER. (1981). Resolution effect on the stereological estimation of surface and volume and its interpretation in terms of fractal dimensions. *J Microsc* **121,** 51-63.

Percie du Sert N, Hurst V, Ahluwalia A, Alam S, Avey MT, Baker M, Browne WJ, Clark A, Cuthill IC, Dirnagl U, Emerson M, Garner P, Holgate ST, Howells DW, Karp NA, Lazic SE, Lidster K, MacCallum CJ, Macleod M, Pearl EJ, Petersen OH, Rawle F, Reynolds P, Rooney K, Sena ES, Silberberg SD, Steckler T & Würbel H. (2020). The ARRIVE guidelines 2.0: Updated guidelines for reporting animal research. *Experimental Physiology* **105,** 1459-1466.

Peterzol A, Bravin A, Coan P & Elleaume H. (2003). Image quality evaluation of the angiography imaging system at the European synchrotron radiation facility. *Nuclear Instruments and Methods in Physics Research Section A: Accelerators, Spectrometers, Detectors and Associated Equipment* **510,** 45-50.

Porzionato A, Guidolin D, Macchi V, Sarasin G, Grisafi D, Tortorella C, Dedja A, Zaramella P & De Caro R. (2016). Fractal analysis of alveolarization in hyperoxia-induced rat models of bronchopulmonary dysplasia. *Am J Physiol Lung Cell Mol Physiol* **310,** L680-688.

Prisk GK, Elliott AR, Guy HJ, Verbanck S, Paiva M & West JB. (1998). Multiple-breath washin of helium and sulfur hexafluoride in sustained microgravity. *J Appl Physiol (1985)* **84,** 244-252.

R CT. (2020). R: A Language and Environment for Statistical Computing. R Foundation for Statistical Computing, Vienna, Austria.

Rodriguez M, Bur S, Favre A & Weibel ER. (1987). Pulmonary acinus: geometry and morphometry of the peripheral airway system in rat and rabbit. *The American journal of anatomy* **180,** 143-155.

Sapoval B, Filoche M & Weibel ER. (2002). Smaller is better--but not too small: a physical scale for the design of the mammalian pulmonary acinus. *Proc Natl Acad Sci U S A* **99,** 10411-10416.

Suortti P, Fiedler S, Bravin A, Brochard T, Mattenet M, Renier M, Spanne P, Thomlinson W, Charvet AM, Elleaume H, Schulze-Briese C & Thompson AC. (2000). Fixed-exit monochromator for computed tomography with synchrotron radiation at energies 18-90 keV. *J Synchrotron Radiat* **7,** 340-347.

Swan AJ & Tawhai MH. (2011). Evidence for minimal oxygen heterogeneity in the healthy human pulmonary acinus. *J Appl Physiol (1985)* **110,** 528-537.

Tanabe N, Sato S, Suki B & Hirai T. (2020). Fractal Analysis of Lung Structure in Chronic Obstructive Pulmonary Disease. *Frontiers in physiology* **11,** 603197.

Tsuda A, Rogers RA, Hydon PE & Butler JP. (2002). Chaotic mixing deep in the lung. *Proc Natl Acad Sci U S A* **99,** 10173-10178.

Valind SO, Rhodes CG, Brudin LH & Jones T. (1991). Measurements of regional ventilation pulmonary gas volume: theory and error analysis with special reference to positron emission tomography. *Journal of nuclear medicine : official publication, Society of Nuclear Medicine* **32,** 1937-1944.

Venegas JG & Galletti GG. (2000). Low-pass filtering, a new method of fractal analysis: application to PET images of pulmonary blood flow. *J Appl Physiol (1985)* **88,** 1365-1373.

Verbanck S & Paiva M. (2011). Gas mixing in the airways and airspaces. *Compr Physiol* **1,** 809-834.

West BJ, Bhargava V & Goldberger AL. (1986). Beyond the principle of similitude: renormalization in the bronchial tree. *J Appl Physiol (1985)* **60,** 1089-1097.

West GB, Brown JH & Enquist BJ. (1997). A general model for the origin of allometric scaling laws in biology. *Science* **276,** 122-126.

West GB, Woodruff WH & Brown JH. (2002). Allometric scaling of metabolic rate from molecules and mitochondria to cells and mammals. *Proc Natl Acad Sci U S A* **99 Suppl 1,** 2473-2478.

Tables

Table 1. Breathing manoeuver characteristics

in vivo	n	t_{insp} (s)	$Flow_{insp}$ (ml/s)	$Volume_{insp}$ (ml)
SBW	16	10.1 ± 2.0	4.8 ± 0.8	48.0 ± 7.8
MBW	16	0.8 ± 0	53.4 ± 11.2	42.7 ± 9.0
post mortem				
SBW	16	10.0 ± 2.0	4.0 ± 0.7	40.0 ± 10.9
MBW	15	0.8 ± 0	44.8 ± 13.4	35.8 ± 10.8
slow-SBW-BH	10	8.0 ± 0.1	3.8 ± 0.8	30.7 ± 6.4
fast-SBW-BH	10	0.8 ± 0	37.9 ± 10.4	30.1 ± 8.3

Data are mean ± SD; t_{insp}, inspiratory time, $Flow_{insp}$, inspiratory flow and $Volume_{insp}$, inspired volume. n: number of manoeuvres obtained from 8 rabbits (SBW, MBW) in vivo and post-mortem, or from 5 rabbits post-mortem (slow-SBW-BH and fast-SBW-BH).

Figures

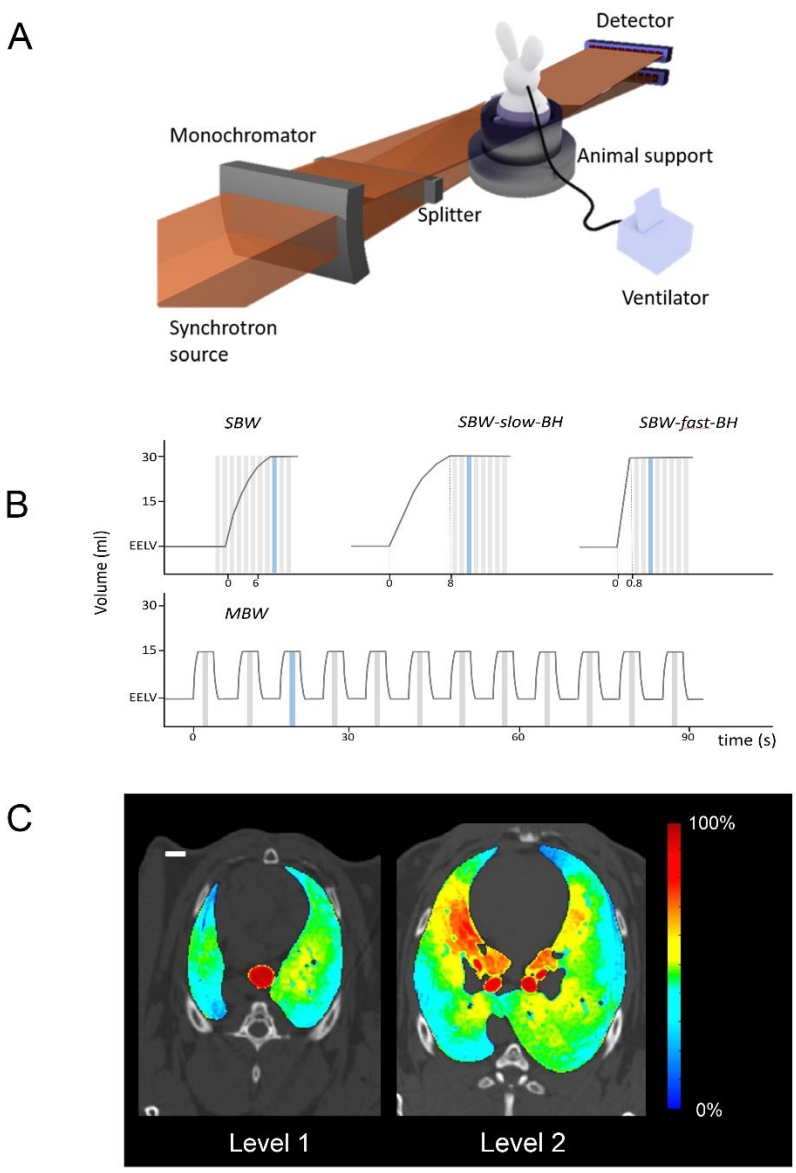

Figure 1. *A*, Schematic of synchrotron radiation K-edge subtraction imaging setup; *B*, Schematic representation of the single-breath Xe inhalation or washin (SBW) manoeuvre, taken as reference, and the multiple-breath washin (MBW) manoeuvre. Also performed in a subset of animals post mortem, a slow and fast inhalation manoeuvre, followed by a breath-hold (SBW-slow-BH; SBW-fast-BH). Grey bars indicate where K-edge subtraction CT images were acquired, blue bars indicate images included in the fractal analysis shown in Figures 4-6. *C*, sample composite images showing the relative Xe concentration distribution corresponding to SBW breathing manoeuvres at 2 axial image levels 1 ("apical") and 2 ("basal").

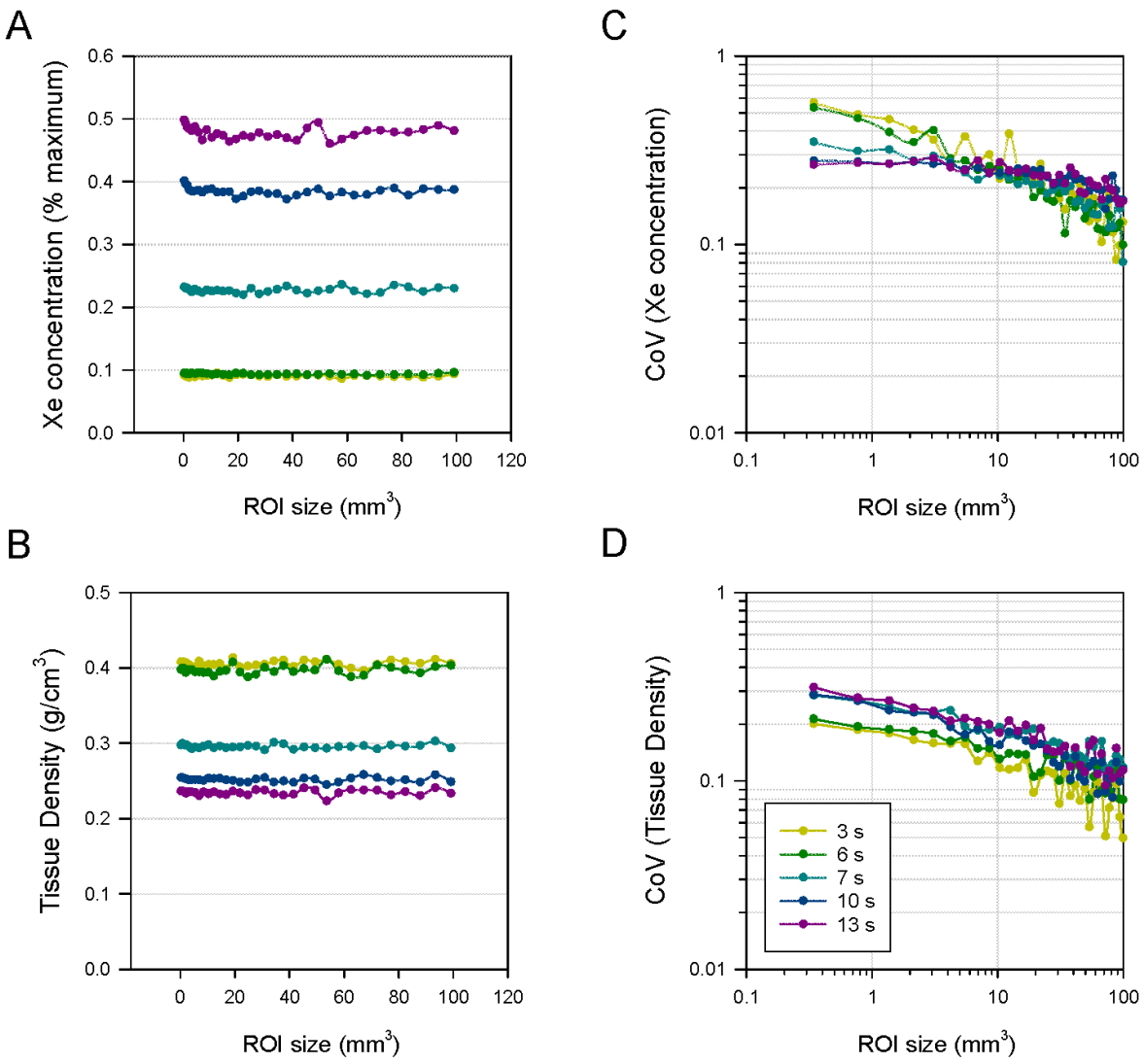

Figure 2. Evolution of Xenon and tissue density curves during the inhalation phase of a typical SBW manoeuvre in a representative animal. *A, B,* Average values of Xe concentration and tissue density across all ROI sizes (L1, *in vivo*); *C, D,* corresponding spatial heterogeneity expressed as Coefficient of Variation in log-log plots. Actual lung inflation starts between the 1 s and 4 s images, and the image at end of inspiration (13 s; violet) are used for the fractal analysis.

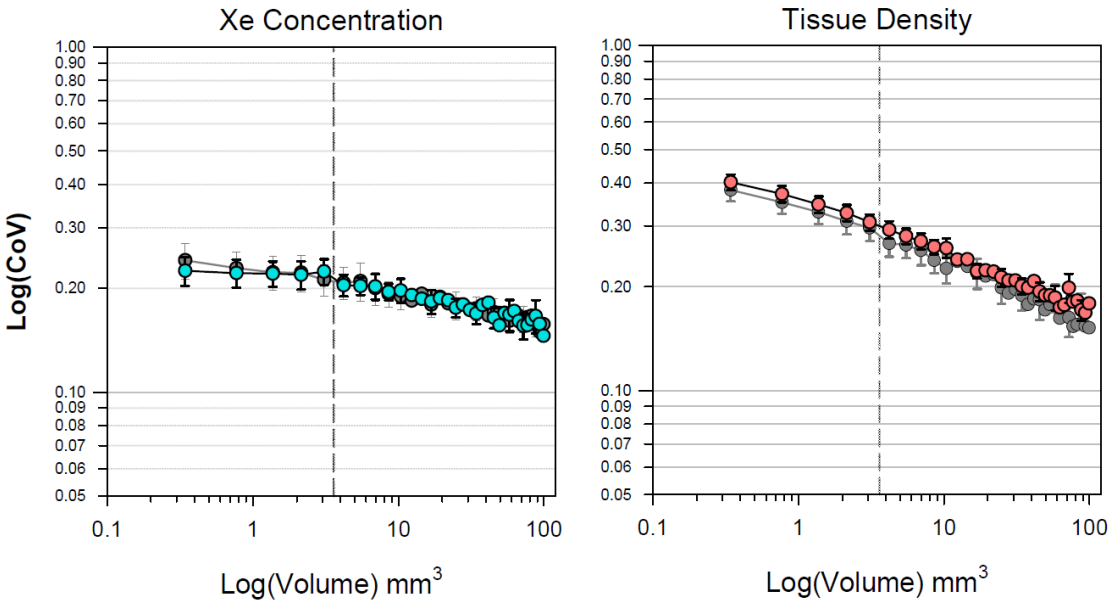

Figure 3. Logarithmic plots of CoV (mean±SD, n=8) of regional Xe concentration (left) and tissue density (right) versus Log region of interest (ROI) volume in axial level 1 images, *in vivo* for the reference SBW manoeuvre. Grey symbols represent axial level 2 data. Dashed line represents the mean cutoff (α) corresponding to 3.8 mm^3 for Xe, replicated in the tissue-density image for comparison. Note the flattening of the curve for ROI volumes below this cutoff for Xe, which is not observed for tissue-density.

A

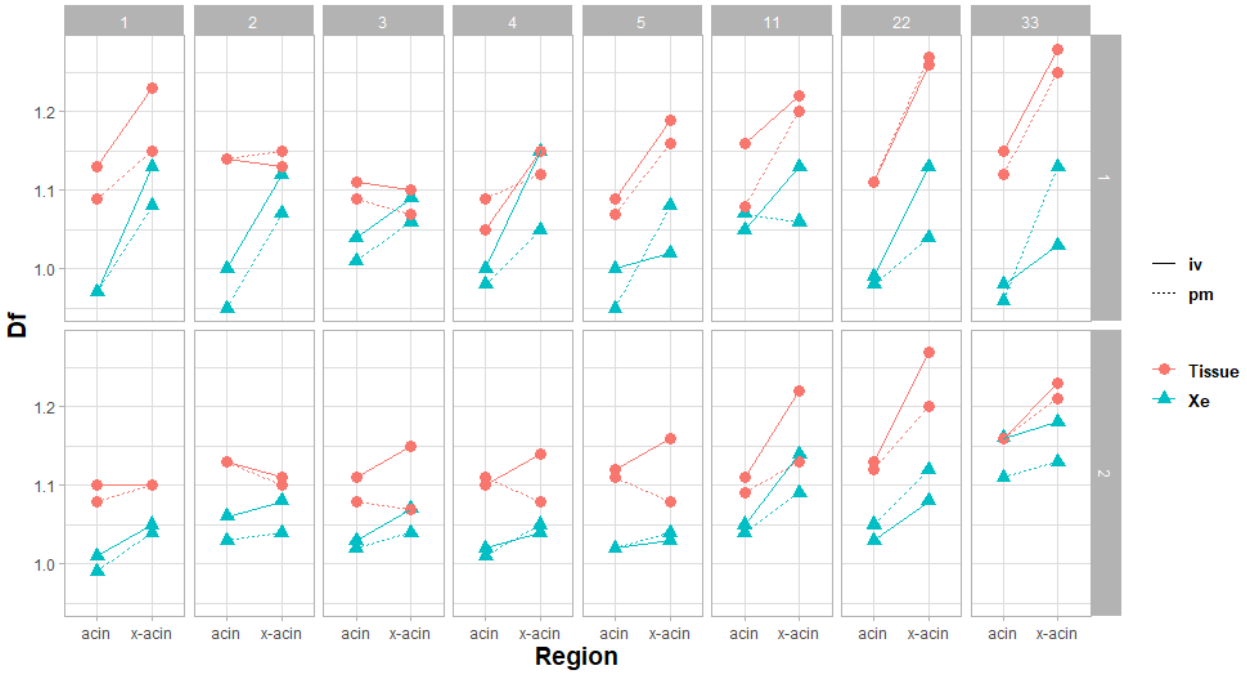

B

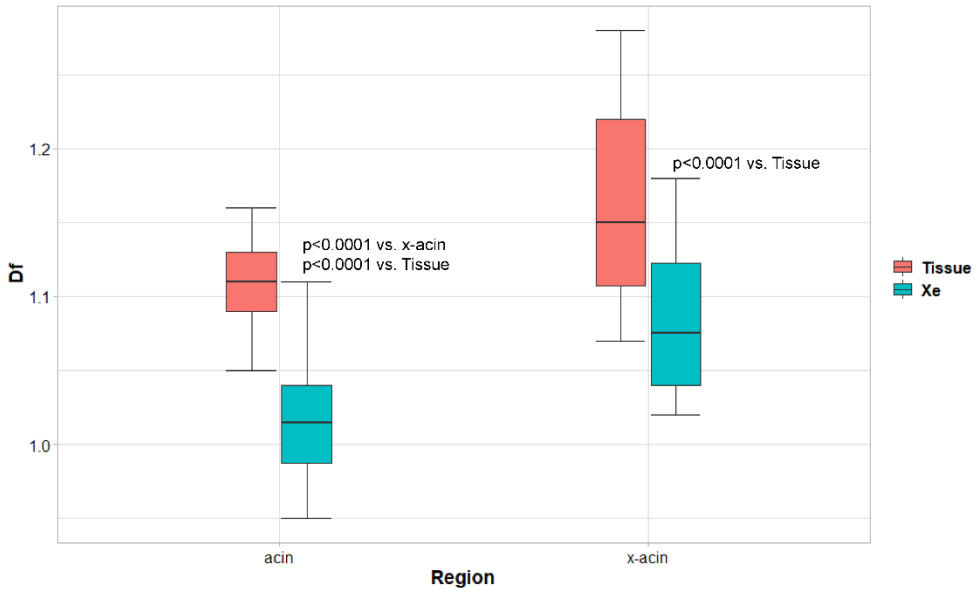

Figure 4. *A*, fractal dimension (D_f) of Xe concentration and tissue-density in individual animals within acinar (acin) and extra-acinar (x-acin) regions and in the 2 axial image levels (level1 and 2), in both in vivo (iv) and post mortem (pm) conditions; *B*, boxplot of averaged data (n=32 for each box; 8 animals×2 levels×2 conditions: *in vivo, post-mortem*).

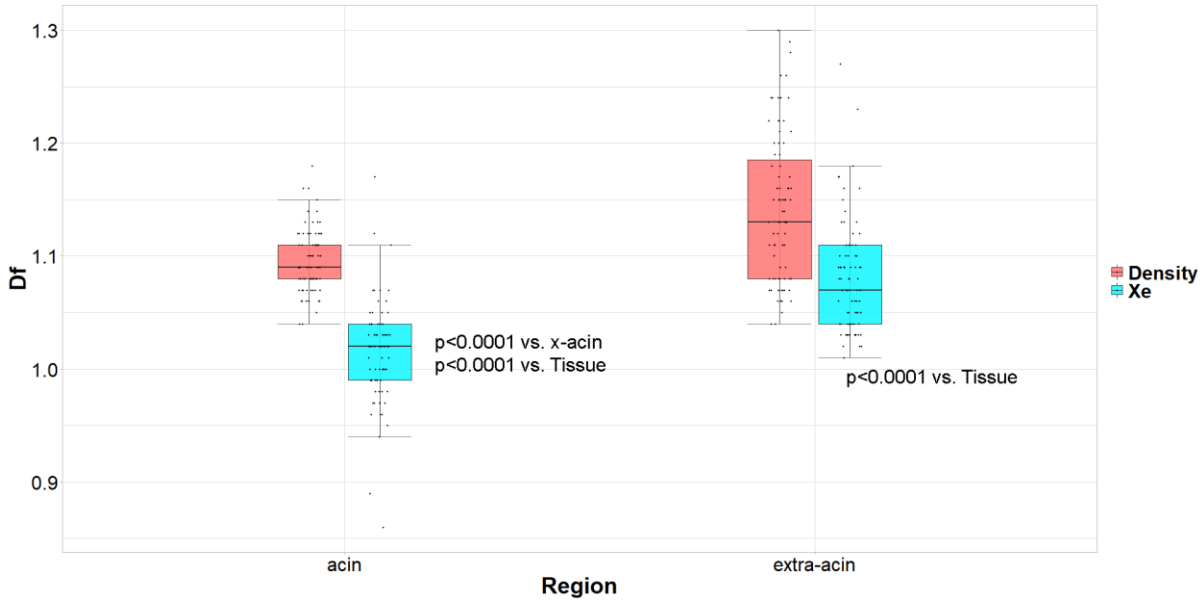

Figure 5. boxplot of averaged data including all breathing manoeuvres SBW, MBW, SBW-slow-BH, SBW-fast-BH (n=83 for each box).

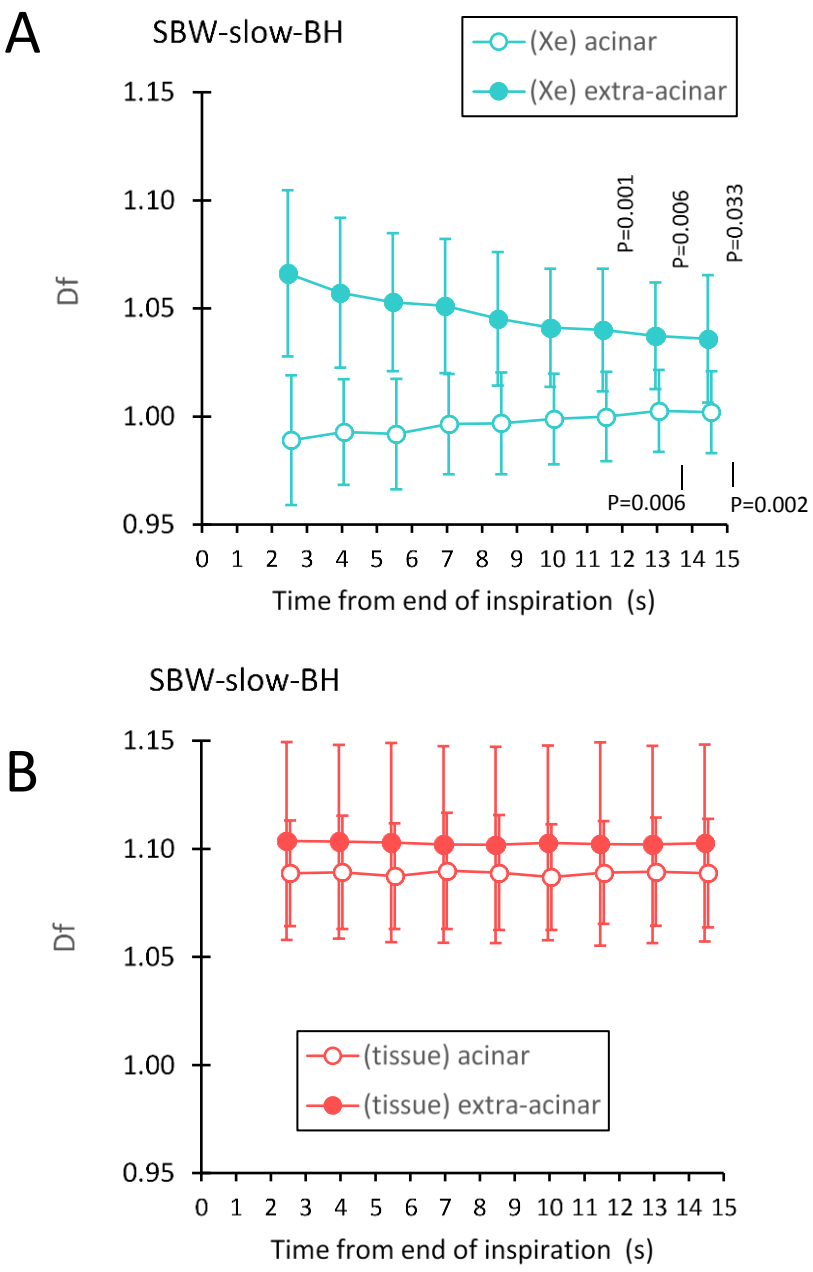

Figure 6. Time evolution from start of end of inspiration of $D_{f,Xe}$ (A) and $D_{f,tissue}$ (B) within acinar and extra-acinar regions in *slow-SBW-BH manoeuvres,* where Xe inhalation was followed by an inspiratory breath hold while images were acquired. Data are m±SD, n=10 per data point (5 animals × 2 image levels). Note the drop in $D_{f,Xe}$ with time within extra-acinar regions while conversely, $D_{f,Xe}$ approached 1.0 within the acinar regions. No significant change was observed in $D_{f,tissue}$.

Supporting Information

Supporting Videos

Video S1: Time-evolution of normalized Xe concentration distribution in a selected axial lung image obtained by synchrotron K-edge subtraction imaging.

Video depicting the time-evolution of normalized Xe concentration during inhalation of 100 % Xe. Images were acquired at 1.5 s intervals during continuous inhalation followed by a short pause, in axial image level 2, shown in Figure 1C. Scale bar represents 10 mm.